



Article

Composition and Geochemical Characteristics of Pyrite and Quartz: Constraints on the Origin of the Xinjiazui Gold Deposit, Northwestern Margin of the Yangtze Block, China

Ji Liu ¹, Xinshang Bao ^{2,*}, Yongbao Gao ¹, Ke Yang ¹, Shaolei Kou ¹, Wei Yang ¹, Zhanbin Wang ¹, Jinglong He ¹, Yixiang Zhang ¹ and Hao Chen ¹

¹ Xi'an Center of Mineral Resources Survey, Xi'an 710100, China; liuji@mail.cgs.gov.cn (J.L.); gyongbao@mail.cgs.gov.cn (Y.G.); yangke01@mail.cgs.gov.cn (K.Y.); koushaolei@mail.cgs.gov.cn (S.K.); yangwei01@mail.cgs.gov.cn (W.Y.); xinjiazui@sina.com (Z.W.); hejinglong@mail.cgs.gov.cn (J.H.); zhangyixiang@mail.cgs.gov.cn (Y.Z.); chenhao01@mail.cgs.gov.cn (H.C.)

² School of Earth Sciences and Resources, Chang'an University, Xi'an 710054, China

* Correspondence: xsbao123@chd.edu.cn

Abstract: The Xinjiazui gold deposit, a newly discovered deposit, is situated in the northwestern margin of the Yangtze Block, China. The source and genesis of gold mineralization are poorly understood. It is urgent to use the H–O isotopic composition of quartz and geochemistry of pyrite to evaluate the origins of the Au and ore-forming fluids of this deposit. Three types of pyrite were identified, including synsedimentary framboidal pyrites (Py0), the directional arrangement of pyrites in pre-mineralization stage (Py1), and euhedral coarse-grain pyrites in the quartz–sulfide veins of the mineralization stage (Py2). The As content in Py2 is relatively higher than Py0 and Py1, indicating that the ore-forming fluids are strongly enriched in As. The $\delta^{34}\text{S}$ values of Py2 (+5.50–+13.34‰) overlap with the S_{1-2}M phyllite (+7.25‰–+8.70‰). This result is consistent with the Pb isotopic composition of Py2, showing that the source of ore-forming materials was derived from the S_{1-2}M phyllite. Meanwhile, the variations in quartz's H and O isotopic composition suggest that the ore-forming fluids were derived originally from metamorphic fluid. Additionally, the Au mineralization is strictly controlled by the shear zone. Above all, we would like to classify the Xinjiazui deposit as an orogenic gold deposit.

Keywords: S–Pb isotopes of pyrite; H–O isotopes of quartz; metal source; deposit genesis; Xinjiazui gold deposit; northwestern margin of the Yangtze Block



Citation: Liu, J.; Bao, X.; Gao, Y.; Yang, K.; Kou, S.; Yang, W.; Wang, Z.; He, J.; Zhang, Y.; Chen, H. Composition and Geochemical Characteristics of Pyrite and Quartz: Constraints on the Origin of the Xinjiazui Gold Deposit, Northwestern Margin of the Yangtze Block, China. *Minerals* **2022**, *12*, 688. <https://doi.org/10.3390/min12060688>

Academic Editor: António Manuel Nunes Mateus

Received: 13 April 2022

Accepted: 26 May 2022

Published: 29 May 2022

Publisher's Note: MDPI stays neutral with regard to jurisdictional claims in published maps and institutional affiliations.



Copyright: © 2022 by the authors. Licensee MDPI, Basel, Switzerland. This article is an open access article distributed under the terms and conditions of the Creative Commons Attribution (CC BY) license (<https://creativecommons.org/licenses/by/4.0/>).

1. Introduction

Orogenic gold deposits are an essential type of global gold deposit, with wide formation ages, wide occurrence depth, high grade, and large scale, accounting for more than 30% of global gold resources [1]. They have also become the research focus of mineral deposit and geotectonic studies [2–4]. In China, most orogenic gold deposits are structurally hosted in metamorphic rocks, with lodes existing as quartz–carbonate veins or veinlets, and gold commonly occurs as disseminations in hydrothermal sulfides in the surrounding area's rocks [5]. However, some significant issues, including the sources of ore-forming components (e.g., fluids, metals, sulfur) of these gold deposits, have been debated for decades [6–10]. Pyrites (FeS_2) are typical major mineral phases and are known for their close association with Au in gold deposits [11–15]. Their texture, chemical, and isotopic variations make them ideal ore-forming condition indicators [11,16–18] and the genesis for various metallic deposits [19–28]. Moreover, the isotopic systems (such as H–O) with specific differences in different geological reservoirs are an important means to define the source of ore-forming materials and ore-forming fluids, and play a vital role in indicating and discriminating the genetic types of ore deposits [6,29–36]. Therefore, the composition

of pyrite and the H–O isotopic composition of quartz veins may provide new information for the debate regarding the origins of Au and ore-forming fluids of the gold deposits.

The Longmenshan orogenic belt, located in the northwestern margin of the Yangtze block, is surrounded by Bikou terrane, South Qinling orogenic belt, Songpan–Garze block, and Hannan–Micangshan tectonic belt [37] (Figure 1b). This orogenic belt consists of several gold deposits, such as the Dingjialin, Taiyangping, Dongjiayuan [38–40], and Xinjiazui gold deposits. The ore-hosting strata of the Dingjialin, Taiyangping, and Dongjiayuan gold deposits are Silurian Maoxian group ($S_{1-2}M$) sericite phyllite [38–40] (Figure 2a). However, the ore body of the Xinjiazui gold deposit is mainly distributed in Cambrian Niutitang formation (ϵ_1n) carbon–silicon–slate, and a small amount in $S_{1-2}M$ phyllite [41] (Figure 3a–c). Although the Xinjiazui gold deposit exhibits a close spatial association with the Dingjialin–Taiyangping metallogenic belt, it is unclear whether they were formed in the same metallogenesis. Therefore, it is critical to compare the source of ore-forming metals and fluids between the Xinjiazui gold deposit and Dingjialin–Taiyangping metallogenic belt.

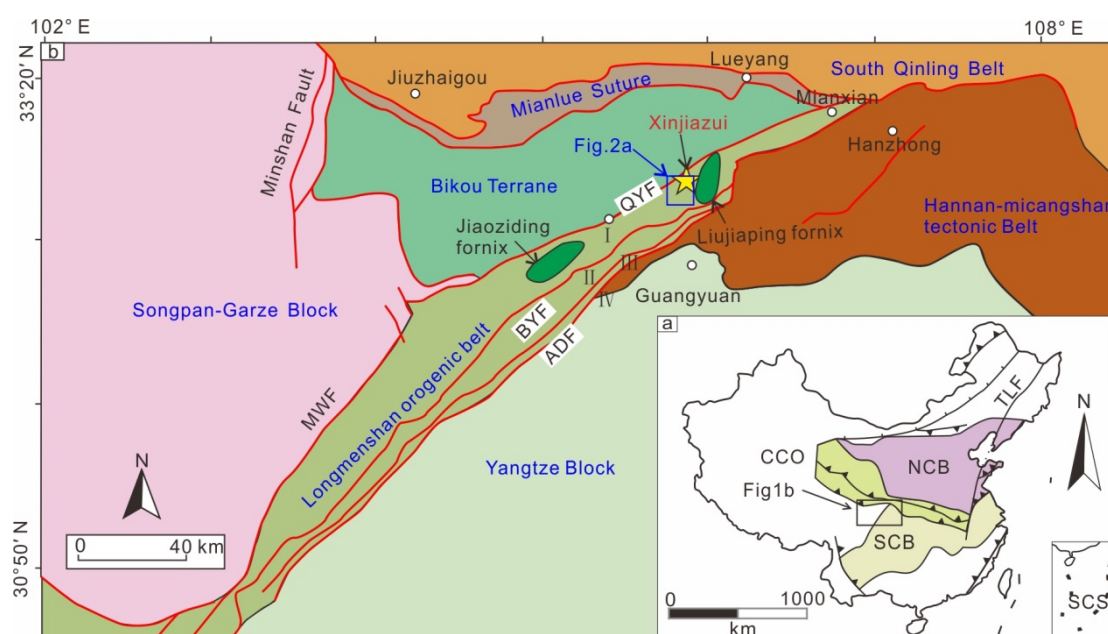


Figure 1. Simplified geotectonic map of the Longmenshan orogenic belt [37,42,43]. (a): regional geological map of the Longmenshan tectonic belt and its adjacent areas; (b): the schematic tectonic map of China and the location of the Longmenshan Orogen. Notes: I. Back Longmenshan orogenic belt; II. front Longmenshan fold and thrust belt; III. Anxian–Dujiangyan fault zone; IV. foreland fold belt. Abbreviations: CCO: Center China Orogen; NCB: North China Block; SCB: South China Block; SCS, South China Sea; TLF: Tancheng–Lujiang Fault; ADF: Anxian–Dujiangyan fault; BYF: Beichuan–Yingxiu fault; QYF: Qingchuan–Yangpingguan fault.

The mineralization of primary ores in the Xinjiazui gold deposit is dominated by quartz-vein-type gold ores, and the gold is mainly hosted by pyrite [41]. Therefore, we chose the quartz-vein-type gold ores as the focus of our study and carried out detailed petrographic observation. Meanwhile, new data from this study include the electron probe component analysis, S and Pb isotopes of the primary gold-bearing pyrites, and the H and O isotopic composition of quartz. The results and new findings are reported in the paper.

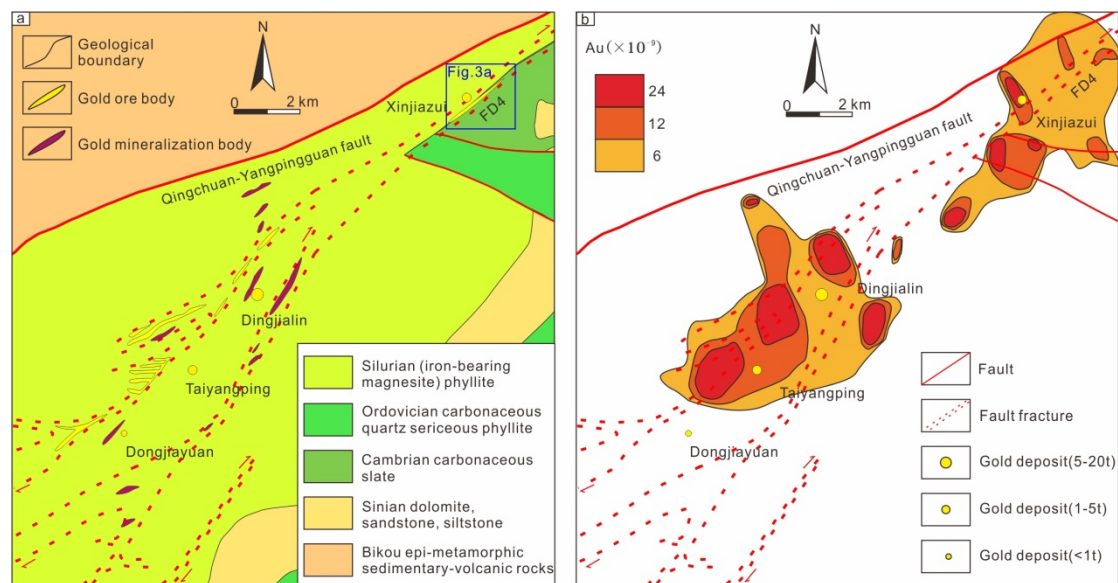


Figure 2. Regional geological map (a) and gold anomalies from stream sediment geochemistry (b) of the Xinjiazui–Dingjialin–Dongjiayuan gold metallogenic belt (modified from 1: 200,000 Bikou geological map; Fu et al., 2014 [40]).

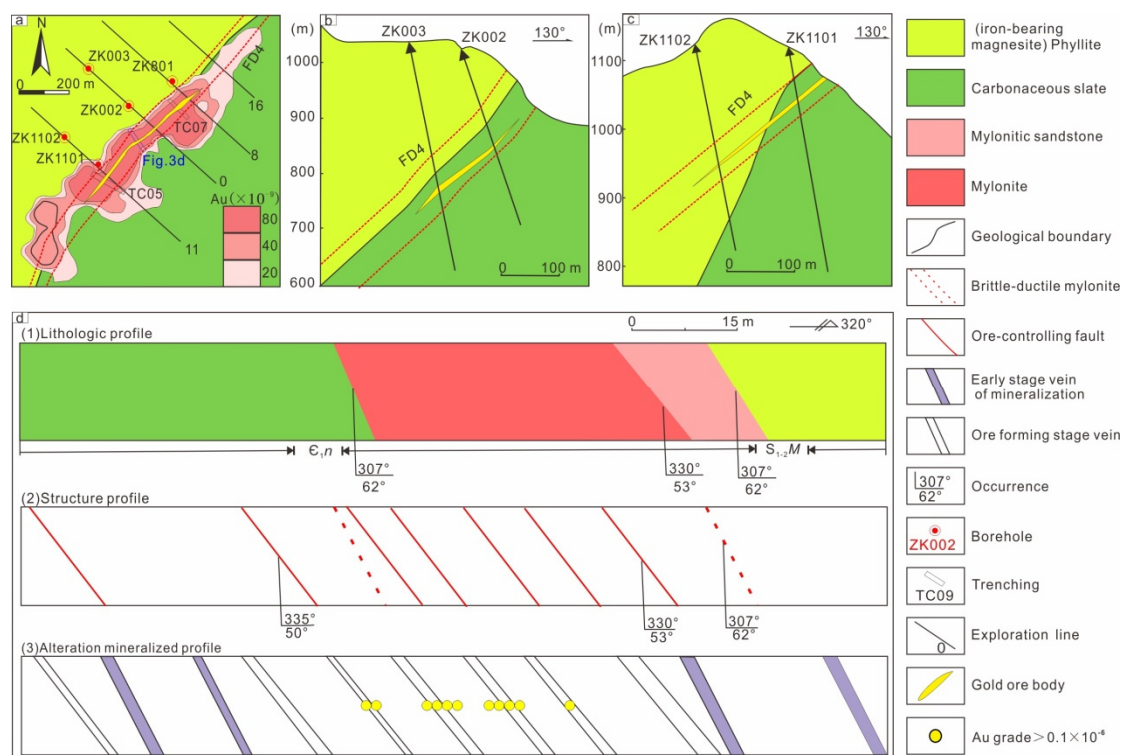


Figure 3. Deposit geology and soil geochemistry (a), exploration line section (b,c), and cross-section of the exploratory trench TC09 (d) in the Xinjiazui gold deposit (Liu et al., 2022 [41]).

2. Regional Geology

The NE-trending Longmenshan thrust–nappe belt formed during the Indosinian collision of the Songpan–Garze block and Yangtze block. Before the Late Triassic, the western margin of the Yangtze block was generally a stable continental marginal development stage, while the Songpan–Garze area was a residual ocean [43]. In the early Indosinian period, the Yangtze Block, Longmen Mountain, and the Songpan–Garze area experienced

a tectonic reversal, which caused the tectonic environment to change from early extension to compression. At this time, the Qingchuan–Yangpingguan fault on the western margin of the Yangtze Block also reversed from an early tensile normal fault to a ductile left-lateral strike-slip. These structural inversions resulted in the westward intracontinental subduction of the Yangtze Block along the Beichuan–Yingxiu fault. Meanwhile, the Qingchuan–Yangpingguan fault, Beichuan–Yingxiu fault, and Anxian–Dujiangyan fault divide the northern segment of Longmenshan orogen and its immediate area into four parts, namely the back Longmenshan orogenic belt (I), front Longmenshan fold and thrust belt (II), Anxian–Dujiangyan fault zone (III), and foreland fold belt (IV) [37] (Figure 1b).

The Qingchuan–Yangpingguan fault is a boundary fault that separates the Back–Longmenshan Orogenic belt and Bikou terrane (Figure 1b), which contains multiple secondary faults, such as the Dingjialin–Taiyangping brittle-ductile shear zone (Figure 2). The Dingjialin to Taiyangping brittle-ductile shear fault, trending 40° – 50° and dipping 50° – 60° , controls the distribution of several gold deposits, such as the Dingjialin, Taiyangping, and Dongjiayuan deposits (Figure 2).

3. Deposit Geology and Mineralization

3.1. Geology of the Xinjiazui Gold Deposit

The Xinjiazui gold deposit is located 8 km northeast of the Dingjialin–Taiyangping gold belt (Figure 2b). The strata in the area mainly consist of Upper Sinian Dengying formation (Z_2^{dn}), Lower Cambrian Niutitang formation (C_1^{nt}), and Silurian Maoxian group (S_{1-2}^M). The ore body of the Xinjiazui gold deposit is vein-like, occurs in Yanzibian–Huashigou brittle-ductile shear fault (FD4), and was distributed in Silurian Maoxian group (S_{1-2}^M) and Cambrian Niutetang formation (C_1^{nt}) strata (Figure 3a–c), with a trend of 315° – 320° and dip angle of 35° – 65° . The ore body has a clear boundary with the surrounding rocks, with an average thickness of 3.53 m and an average grade of 2.90×10^{-6} . Notably, the Yanzibian–Huashigou shear fault strictly controls the ore mineralization, and high-grade gold ores are developed only in the position with ductile solid deformation and brittle fracture (Figure 3d).

The mineralization of primary ores in the Xinjiazui gold deposit is dominated by quartz-vein-type gold ores. Gold is mainly hosted by pyrite, quartz, and a small amount of polymetallic sulfides, and it occurs as fracture gold or gold inclusions. The fracture gold (2–10 μm) is mainly distributed in the fractures of pyrite in the form of branching, wheat grain, and veined gold. The gold inclusions (2–8 μm) are embedded in pyrite or hematite in irregular granular and rounded form. Combining the crosscutting relationship of veins, the characteristics of mineral paragenetic association, and typical ore fabric, the mineralization of the Xinjiazui gold deposit can be divided into hydrothermal mineralization and supergene oxidation epoch. The hydrothermal metallogenic epoch is the primary ore event. It can be subdivided into three stages: (I) quartz–pyrite stage, (II) quartz–calcite–natural gold polymetallic sulfide stage, and (III) quartz–carbonate stage [41].

3.2. Texture of Pyrite and Mineral Paragenetic Sequence

Based on petrographic observations and backscattered electron (BSE) analysis, pyrites in the Xinjiazui deposit are classified into three generations (Figure 4), including the framboidal pyrites in the synsedimentary epoch (Py0), the directional arrangement of hydrothermal pyrite in pre-mineralization stage (Py1), and coarse grains disseminated in the quartz–sulfide veins of mineralization stage (Py2).

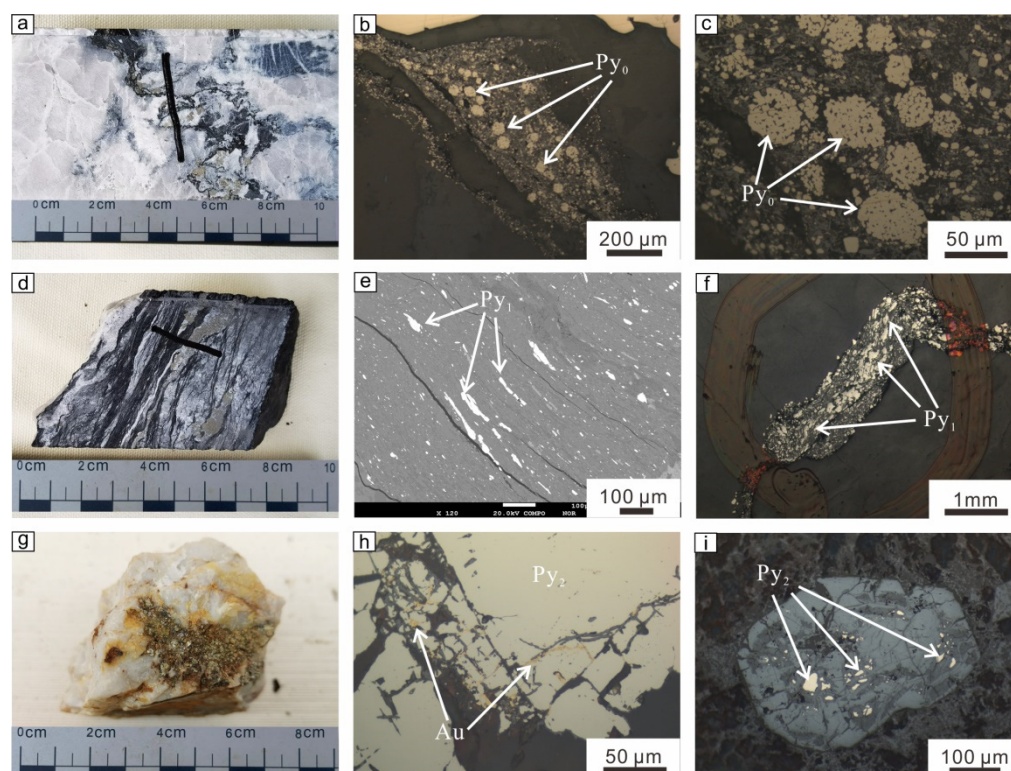


Figure 4. Photographs of three generations of pyrite from the Xinjazui gold deposit. (a) Quartz veins wrapped surrounding rock breccia in the ore-forming stage; (b) framboidal pyrite (Py₀) in breccia of surrounding rock (reflected light); (c) framboidal pyrite (reflected light); (d) the pyrite quartz veins developed along the phyllite in the early stage of mineralization; (e) the pyrite (Py₁) has elongated and drawn wire deformation and oriented arrangement (back scatter); (f) ductile shear deformation occurs in pyrite (Py₁) (reflected light); (g) oxidized gold ores; (h) natural gold is embedded in the pyrite (Py₂) fissures (reflected light); (i) pyrite is oxidized to hematite, which retains the pentagonal dodecahedron crystal form and forms skeleton crystal structure (reflected light).

The framboidal pyrite (Py₀), mainly distributed in a relatively fresh Cambrian carbonaceous slate (Figure 4a–c), is comprised of framboidal grained (about 5 µm) sub-euhedral to anhedral pyrite grains. Locally, the size of framboidal aggregate can be 50 µm. The Py₀ corresponds to the pre-enrichment stage of syngenetic hydrothermal sedimentation.

The Py₁ is mainly produced as quartz–pyrite veins along the phyllite or plate and is formed in the early stage of mineralization, with a particle size of 10–30 µm. The quartz–pyrite veins underwent ductile shear deformation along with the surrounding rock, resulting in the pyrite being elongated and drawn wire-oriented (Figure 4d–f). This stage suffered from regional brittle–ductile shear deformation, conducive to the migration and accumulation of ore-bearing fluids.

The Py₂ is developed in the relatively wide quartz vein or the contact area between the vein and surrounding rocks. These euhedral pyrite grains (Py₂) have a size of 50 µm–2 mm without zoned texture and contain abundant fracture gold or gold inclusions (Figure 4g,h). Notably, some pyrites have a fragmented structure (Figure 4h,i), indicating that this stage has suffered from brittle fracture. Near-surface pyrites were oxidized to hematites, which retained the pentagonal dodecahedron of pyrite, forming a skeleton texture (Figure 4i).

4. Analytical Methods

Electron microprobe (EPMA) analysis: In this paper, EPMA was used to analyze the major elements of 98 spots in pyrite samples from the Xinjazui gold deposit, including 11 spots on Py₀, 35 spots on Py₁, and 52 spots on Py₂. The pyrite’s major and minor element compositions were determined by JXA–8230 electron probe with a WDS detector

at Xi'an Geological Survey Center, China Geological Survey, under 20 kV and 10 nA, with a beam size of 1 μm in diameter. The ZAF correction method was used to correct the atomic number (Z), absorption (A), and fluorescence (F) effects for all analyzed minerals.

S Isotope Analyses of Pyrites in the quartz–sulfide veins of the mineralization stage (Py2) were carried out at Xi'an Ruishi Geological Technology Co., Ltd., Xi'an, China, using the DZ/T0184–1997 method. The instrument includes 253plus, Flash EA elemental analyzer, and Conflo IV multi-purpose interface (American Thermoelectric Company). The Iaea-s3, GBW04414, and GBW04415 were chosen as reference materials, and the analytical accuracy of the standard sample was found to be better than 0.2‰. The $\delta^{34}\text{S}$ analysis was normalized to the Canyon Diablo troilite VCDT value.

Pb Isotope Analyses of Pyrites in the quartz–sulfide veins of mineralization stage (Py2) were completed in the State Key Laboratory of Continental Dynamics, Northwestern University. Pb isotope composition test, consisting of separation and testing, was carried out on the Neptune Plus MC–ICP–MS (ThermoFisher). Firstly, the sample was added to the digestion tank and dissolved with HF and HNO_3 . The dissolved sample was separated with Sr-specific resin (produced by Triskem, Bruz, France). After pre-cleaning and leaching, based on the Pb concentration of the solution, a standard solution of Tl was added so that the ratio of Pb and Tl was 1:1 [44]. All tests were carried out in static mode, $^{202}\text{Hg}^+$ was used to monitor the interference of $^{204}\text{Hg}^+$ to $^{204}\text{Pb}^+$, $^{203}\text{Tl}/^{205}\text{Tl}$ was used as an external standard [45], and the effect of mass fractionation was corrected by $^{203}\text{Tl}/^{205}\text{Tl} = 2.3889$. The Pb isotope ratio was normalized by $^{203}\text{Tl}/^{205}\text{Tl} = 0.418922$.

Hydrogen–Oxygen Isotopes of Quartz in the quartz–sulfide veins of the mineralization stage were analyzed on a 253plus mass spectrometer in the Xi'an Ruishi Geological Technology Co., LTD, China, following the technique described by Gong et al. (2007) [46] and Ding et al. (1994) [47]. The $\delta^{18}\text{O}$ values of ore-forming fluids ($\delta^{18}\text{O}_\text{W}$) were calculated from the $\delta^{18}\text{O}$ values of quartz ($\delta^{18}\text{O}_\text{Q}$). δD values were obtained by measuring fluid inclusions in quartz. Analysis procedures followed those described by Ding et al. (1994) [47]. Isotopic ratios for oxygen and hydrogen are presented in standard δ notation (‰) relative to the Standard Mean Ocean Water (SMOW). Analytical precision was $\pm 0.2\text{‰}$ for $\delta^{18}\text{O}$ and $\pm 1\text{‰}$ for δD , respectively.

5. Results

5.1. Pyrite Chemical Composition

The EPMA results (Table S1) show that the Fe and S contents in Py0 are slightly lower than those in Py1 and Py2 (Table 1). Compared with the theoretical chemical composition of pyrite (Fe and S are 46.55% and 53.45%, respectively), the three types of pyrites (Py0, Py1, and Py2) have the characteristics of lower Fe (averaging 45.42%, 45.79%, 45.92%, respectively) and higher S (averaging 53.69%, 54.14%, 54.08%, respectively). This chemistry indicates that pyrites in the Xinjiazui gold deposit are generally enriched in S (Figure 5a).

Table 1. Electron probe analyses of different types of pyrites in the Xinjiazui gold deposit.

Mineral Generation	Py0 (n = 11)				Py1 (n = 35)				Py2 (n = 52)				D.L.
	MAX	MIN	AVG	STD	MAX	MIN	AVG	STD	MAX	MIN	AVG	STD	
As	0.055	/	0.022	0.019	0.181	/	0.040	0.049	2.228	/	0.202	0.417	421
Se	0.087	/	0.020	0.026	0.089	/	0.028	0.028	0.168	/	0.037	0.052	191
Zn	0.081	/	0.018	0.029	0.075	/	0.016	0.020	0.078	/	0.014	0.021	313
Cu	0.048	/	0.015	0.019	0.055	/	0.014	0.018	0.065	/	0.012	0.016	299
Ni	0.037	/	0.007	0.012	1.018	/	0.106	0.178	0.370	/	0.054	0.077	235
Co	0.112	0.024	0.069	0.029	0.284	/	0.071	0.057	0.600	0.002	0.076	0.093	218
Fe	46.18	44.33	45.42	0.52	46.90	44.50	45.79	0.63	46.64	45.00	45.92	0.43	218
Cr	0.074	/	0.022	0.027	0.043	/	0.010	0.011	3.860	/	0.100	0.535	198
S	54.16	53.30	53.69	0.30	54.81	52.59	54.14	0.47	54.85	52.75	54.08	0.43	67

Table 1. Cont.

Mineral Generation	Py0(n = 11)				Py1(n = 35)				Py2(n = 52)				D.L.
	MAX	MIN	AVG	STD	MAX	MIN	AVG	STD	MAX	MIN	AVG	STD	
Pb	0.115	/	0.046	0.039	0.137	/	0.034	0.046	0.169	/	0.041	0.048	427
Te	0.020	/	0.004	0.007	0.037	/	0.006	0.010	0.053	/	0.008	0.013	160
Sb	0.037	/	0.009	0.013	0.071	/	0.011	0.016	0.050	/	0.009	0.014	171
Total	100.27	97.88	99.38	0.69	101.67	97.90	100.29	0.88	101.77	99.31	100.50	0.60	/

Abbreviations: AVG: average (wt%); MAX: maximum (wt%); MIN: minimum (wt%); STD: standard deviation; D.L.: detection limitation (ppm).

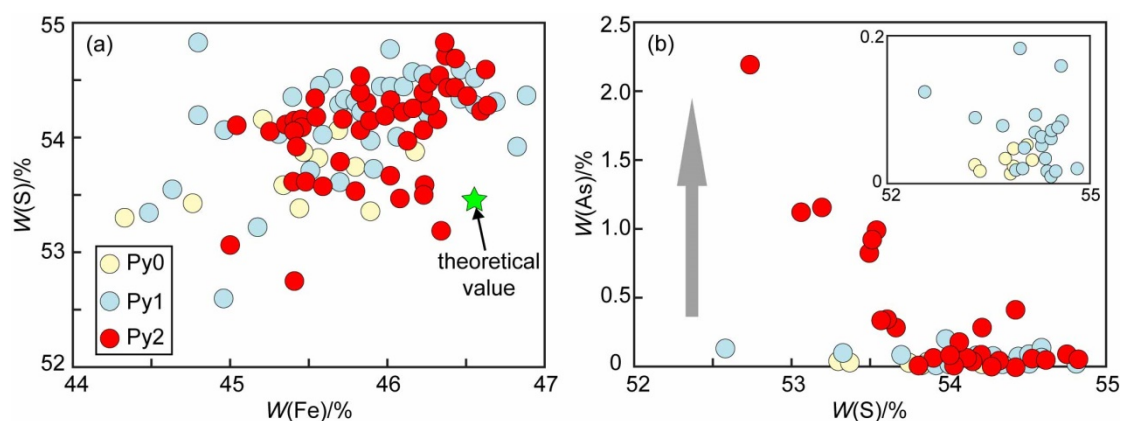


Figure 5. The plots of main elemental contents of pyrites in the Xinjiazui gold deposit, including (a) $w(S)$ vs. $w(Fe)$ and (b) $w(As)$ vs. $w(S)$ diagrams.

Py0 (0.013% to 0.055%) and Py1 (0.007% to 0.181%) contain similar As content, and both are lower than that of Py2 (0.003% to 2.228%, Figure 5b). The variation of As contents reflect the evolution of the ore-forming fluid composition, so the subtle differences in As content of Py0, Py1, and Py2 indicate that the ore-forming fluids are more enriched in As. Moreover, there is an obvious negative correlation between the As and S in pyrite (Figure 5b), suggesting that As replaces S in pyrite [48].

5.2. S and Pb Isotopes

Sulfur isotope compositions of pyrite in Xinjiazui, Dingjialin, and Taiyangping gold deposits are listed in Table 2. As shown, the Py2 exhibits positive $\delta^{34}S$ values ranging from 5.50‰ to 13.34‰, with an average of 10.58‰ and a median of 12.89‰. Moreover, the $\delta^{34}S$ ratios of Py2 have relatively narrow ranges, indicating that the sulfur isotope ratio of pyrite has reached equilibrium. These $\delta^{34}S$ ratios are also similar to the $\delta^{34}S$ ratios of pyrite from the Taiyangping (8.50‰–9.90‰; [38,39]) and Dingjialin gold deposits (6.60‰–10.20‰; [38]).

Lead isotope data ($^{206}Pb/^{204}Pb$, $^{207}Pb/^{204}Pb$, and $^{208}Pb/^{204}Pb$ ratios) of Py2 in the Xinjiazui gold deposit are mainly concentrated in the ranges 18.177–18.204, 15.688–15.696, and 38.595–38.652, respectively (Table 3). On $^{207}Pb/^{204}Pb$ – $^{206}Pb/^{204}Pb$ and $^{208}Pb/^{204}Pb$ – $^{206}Pb/^{204}Pb$ plots, most data are plotted in a field representing the upper crust (Figure 6).

Table 2. Sulfur isotopic composition of pyrite from the Xinjiazui, Dingjialin, and Taiyangping gold deposits.

Sample	Location	Rock	$\delta^{34}S/‰$	Data Source
PD01–11	Xinjiazui	pyritization quartz vein	12.89	This study
PD01–12	Xinjiazui	pyritization quartz vein	13.34	This study
TC09–19–2	Xinjiazui	pyritization quartz vein	5.50	This study
CPD39–26	Dingjialin PD39	$S_{1-2}M$ phyllite	8.70	[38]

Table 2. Cont.

Sample	Location	Rock	$\delta^{34}\text{S}/\text{‰}$	Data Source
PD3–3a	Dingjialin PD3	pyritization quartz vein	6.60	[38]
PD2–5	Dingjialin PD2	pyritization quartz vein	10.20	[38]
V4–1	Taiyangping	pyritization quartz vein	8.50	[38]
V9–1	Taiyangping	pyritization quartz vein	9.90	[38]
V9–2	Taiyangping	pyritization quartz vein	9.30	[38]
PD700H4	Taiyangping	pyritization quartz vein	9.07	[39]
PD792H3	Taiyangping	pyritization quartz vein	9.43	[39]
PD878H6	Taiyangping	pyritization quartz vein	9.84	[39]
PD947H2	Taiyangping	S _{1–2} M phyllite	7.25	[39]
PD947H2/2	Taiyangping	S _{1–2} M phyllite	7.32	[39]

Notes: $\delta^{34}\text{S}$ values were reported relative to the Vienna Cañon Diablo troilite (VCDT). An uncertainty of $\pm 0.2\text{‰}$ is recommended.

Table 3. Lead isotopic compositions of stage II pyrite (Py2) from the Xinjiazui gold deposit.

Sample	Location	Rock	$^{208}\text{Pb}/^{204}\text{Pb}$	$^{207}\text{Pb}/^{204}\text{Pb}$	$^{206}\text{Pb}/^{204}\text{Pb}$
PD01–11	Xinjiazui	pyritization quartz vein	38.652	15.696	18.204
PD01–12	Xinjiazui	pyritization quartz vein	38.596	15.689	18.177
TC09–19–2	Xinjiazui	pyritization quartz vein	38.432	15.674	18.148

Notes: Standard errors are within 0.004 for $^{206}\text{Pb}/^{204}\text{Pb}$, within 0.003 for $^{207}\text{Pb}/^{204}\text{Pb}$, and within 0.007 for $^{208}\text{Pb}/^{204}\text{Pb}$.

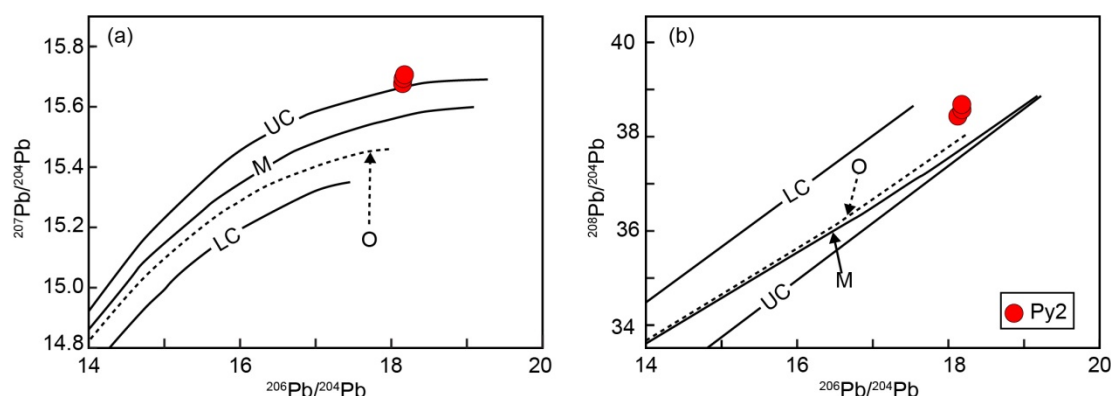


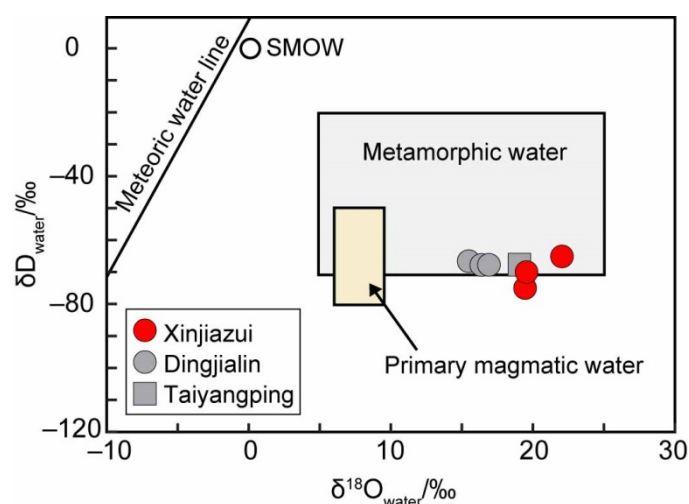
Figure 6. Pb isotopic composition of samples from the Xinjiazui gold deposit plotted with the evolution curve of Zartman and Doe (1981) [49], including (a) $^{208}\text{Pb}/^{204}\text{Pb}$ vs. $^{206}\text{Pb}/^{204}\text{Pb}$ and (b) $^{207}\text{Pb}/^{204}\text{Pb}$ vs. $^{206}\text{Pb}/^{204}\text{Pb}$. LC: lower crust; M: mantle; O: orogen; UC: upper crust.

5.3. Hydrogen and Oxygen Isotopes

Hydrogen and oxygen isotope data are important monitors for the source and evolution of fluids. The H and O isotopic compositions of quartz from the Xinjiazui, Dingjialin, and Taiyangping gold deposits are listed in Table 4. The Xinjiazui gold deposit lacks magmatic activities, which excludes a magmatic source of the ore-forming fluids. The $\delta^{18}\text{O}$ and δD values of ore-forming fluids vary, respectively, from $+19.5\text{‰}$ to $+22.1\text{‰}$ and from -79‰ to -69‰ for the main stage of mineralization in the Xinjiazui gold deposit. These ranges are consistent with the Dingjialin ($\delta^{18}\text{O} = +15.5\text{‰}$ to $+17.1\text{‰}$, $\delta\text{D} = -67\text{‰}$ to -66‰ , [38]) and Taiyangping ($\delta^{18}\text{O} = +18.9\text{‰}$, $\delta\text{D} = -67\text{‰}$, [38]) gold deposits in this region. The reliable δD and $\delta^{18}\text{O}$ ratios of ore-fluids mostly fall close to the lower side of the metamorphic field (Figure 7), possibly with a small amount of meteoric water. The results of these H–O isotope analyses are consistent with the composition range of orogenic gold deposits (H–O isotopes of water-bearing minerals mainly range from -80‰ to -20‰ , and $+6\text{‰}$ to $+13\text{‰}$ [3,6,50]), reflecting that the ore-forming fluid was derived from metamorphic fluid in this region. As for the temperature and salinity of the ore-forming fluids, measuring the temperature of the fluid inclusions in the future will help solve this problem.

Table 4. Oxygen and hydrogen isotopic composition of quartz from the Xinjiazui, Dingjialin, and Taiyangping gold deposits.

Sample	Laocation	Rock	$\delta^{18}\text{O}_{\text{V-SMOW}}(\text{‰})$	$\delta\text{DV-SMOW}(\text{‰})$	$\delta^{18}\text{O}_{\text{V-PDB}}(\text{‰})$	Data Source
PD01–11	Xinjiazui	Sulfide–quartz vein	19.5	−79	−11.0	This study
PD01–12	Xinjiazui	Sulfide–quartz vein	19.6	−73	−10.9	This study
TC09–19–2	Xinjiazui	Sulfide–quartz vein	22.1	−69	−8.5	This study
CPD39–9	Dingjialin	Quartz-bearing microveined phyllite	16.4	−67	−29.0	[38]
CPD39–26	Dingjialin	Sulfide–quartz vein	15.5	−66	−20.4	[38]
PD3–3a	Dingjialin	Sulfide–quartz vein	17.1	−66	−24.5	[38]
V4–1	Taiyangping	Sulfide–quartz vein	18.9	−67	−27.6	[38]

**Figure 7.** $\delta\text{D}_{\text{H}_2\text{O}}$ and $\delta^{18}\text{O}_{\text{H}_2\text{O}}$ values of ore-forming fluids measured or calculated from hydrothermal quartz. Fields for magmatic and metamorphic waters are from Taylor (1973) [31].

6. Discussion

6.1. Source of Sulfur and Metal

These $\delta^{34}\text{S}$ ratios of gold-related pyrites in the Xinjiazui gold deposit (+5.50‰–+13.34‰) are similar to the $\delta^{34}\text{S}$ ratios of pyrite from the Taiyangping (8.50‰–9.90‰ [38,39]) and Dingjialin gold deposits (6.60‰–10.20‰ [38]) (Figure 8), indicating that the same dominant sulfur source for Xinjiazui, Dingjialin, and Taiyangping gold deposits. Positive $\delta^{34}\text{S}$ values reflect the characteristics of formation sulfur. The ore body of the Xinjiazui gold deposit occurs in S_{1-2}M phyllite and E_{1n} carbon–silicon–slate, while the ore bodies of Dingjialin and Yangyangping gold deposits only occur in S_{1-2}M phyllite (Figure 3). The protolith of S_{1-2}M phyllite has the character of turbidite. The turbidite is rich in iron, sulfur, and other gold-loving elements, which is conducive to the pre-enrichment of gold. Importantly, the Maoxian group contains nearby 10.0 ppb Au [51], twice the Clark value (4 ppb [52]), indicating that the S_{1-2}M phyllite has the potential to provide gold for the gold mineralization in the Xinjiazui deposit. However, the S_{1-2}M phyllite shows slightly lighter $\delta^{34}\text{S}$ ratios (+7.25‰–+8.70‰ [38,39]), while the E_{1n} carbon–silicon–slate exhibit heavier $\delta^{34}\text{S}$ ratios (+25‰–+30.5‰ [53]) than that of pyrite in the Xinjiazui deposit. This chemistry indicates that the sulfur source of pyrite in the ore-forming stage of Xinjiazui gold deposit is mainly from S_{1-2}M phyllite. The wide $\delta^{34}\text{S}$ of the Xinjiazui gold deposit is probably related to minor sulfur additions from the E_{1n} carbon–silicon–slate.

In the main stage of the Xinjiazui gold deposit, pyrite is closely related to gold and is the main gold-bearing mineral [41], indicating that pyrite and gold were formed in the same fluid system, and the lead isotope of pyrite (Py2) can reflect the source region of gold [54]. The $^{206}\text{Pb}/^{204}\text{Pb}$, $^{207}\text{Pb}/^{204}\text{Pb}$, and $^{208}\text{Pb}/^{204}\text{Pb}$ ratios of Py2 changed little, and were relatively stable in the ore-forming stage, indicating that the source of ore-forming materials in the area was consistent. Pyrite (Py2) lead isotopes are all located in the upper

crust (Figure 6a) and concentrated along and above the evolution line of the orogenic belt (Figure 6b), showing the characteristics of orogenic lead isotopes.

6.2. Deposit Type

The Xinjiazui gold deposit is located in the junction area of the Yangtze Block, Bikou terrane, South Qinling orogenic belt, and Songpan–Garze block. The NE-trending Qingchuan–Yangpingguan ductile-brittle shear fault strictly controls Au mineralization distribution, shape, and occurrence. The gold orebodies mainly occur in the Yanzibian–Huashigou fault, a secondary fault of the Qingchuan–Yangpingguan ductile-brittle shear fault (Figures 2 and 3). Most of the orebodies are NE-trending “entering”-type auriferous quartz complex vein, and high-grade gold ores are developed only in the position with strong ductile deformation and brittle fracture (Figure 3d). Thus, the Xinjiazui deposit is controlled by ductile-brittle shear fault and brittle fracture [41].

Above all, the Xinjiazui gold deposit is considered to be an orogenic gold deposit, the characteristics of which are similar to those of typical examples [3,5,6,55–57]:

- (1) The deposit occupies a spatial and temporal position consistent with the Longmen-shan Orogen, a collisional orogenic belt;
- (2) The wall rocks were deformed and metamorphosed to phyllite or slate;
- (3) Mineralization is not stratigraphically selective. Ductile shear zone and brittle fracture structurally controlled the Au mineralization;
- (4) Pyrite is the dominant sulfide mineral in the ores, and gold is mainly hosted in pyrite as fracture gold or gold inclusions;
- (5) The ores exhibit a simple element assemblage of Au(–Ag), and gold occurs in the form of native gold;
- (6) Sulfur and gold were derived from the shallow metamorphic and strongly deformed sedimentary rock series ($S_{1-2}M$);
- (7) The ore-forming fluids had a metamorphic source.

6.3. Mechanism of Mineralization

Based on the analyses presented in this paper, together with previous studies [38], a genetic model has been constructed for the Xinjiazui deposit (Figure 9). Metallogenic materials of the Xinjiazui gold deposit mainly come from the surrounding rock (Figures 6 and 8), and gold pre-enrichment occurs during the deposition and diagenesis of the original surrounding rock (Figure 9a). After the Qingchuan–Yangpingguan fault entered the Silurian Maoxian formation, a series of brittle and ductile shear faults were produced, such as the Yanzibian–huashigou ductile-brittle shear fault. Deep metamorphic fluids move upward along the ductile–brittle shear fault and extract metallogenic material from the surrounding rocks ($S_{1-2}M$ phyllite and ϵ_{1n} carbon–silicon–slate) through water–rock exchange. Furthermore, they then lead to the element Au being remobilized, forming Au-bearing tectonic-metamorphic hydrothermal fluids (Figure 9b). Moreover, the superposition of brittle fractures in the later stage leads to the further enrichment of gold and other metal-forming materials, and high-grade gold ore is finally formed at the superposition of strong ductile deformation and brittle fractures (Figure 9c). It can be seen that natural gold (electrum) occurs in pyrite in the form of fracture gold or gold inclusions (Figure 4h).

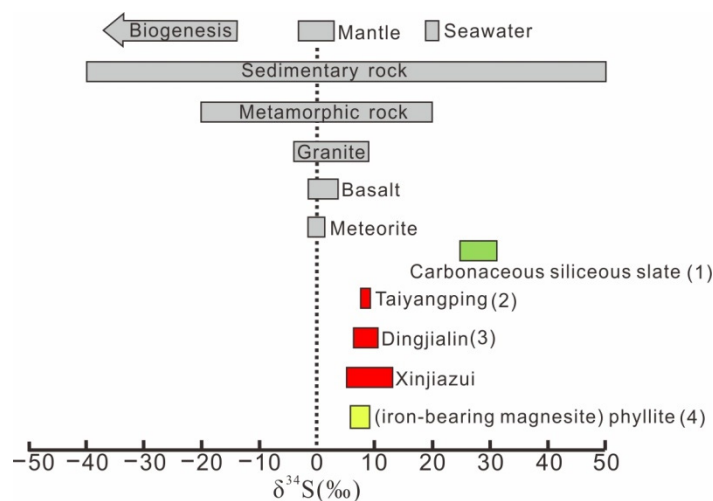


Figure 8. Box-plots of $\delta^{34}\text{S}$ values of ore-forming pyrites from the Xinjiazui, Taiyangping, and Dingjialin gold deposits. Base map modified after Zheng et al. (2000) [58]; data sources of pyrite $\delta^{34}\text{S}$ values for Carbonaceous siliceous slate are from Zuo (2020) [53]; those for Taiyangping deposit and phyllite are both from Wei (2008) and Zhong (2012) [38,39]; those for Dingjialin deposit are from Wei (2008) [38].

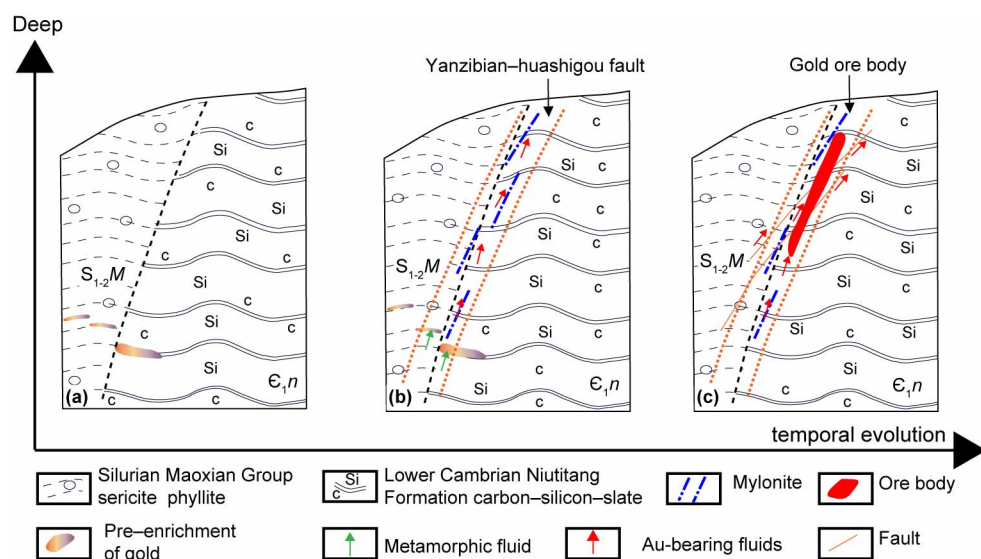


Figure 9. Superimposition model for ore mineralization in the brittle-ductile shear zone in the Xinjiazui gold deposit. (a) gold pre-enrichment occurs during the deposition and diagenesis of the original surrounding rock; (b) deep metamorphic fluids move upward along the ductile–brittle shear fault and lead to the element Au being remobilized, forming Au-bearing tectonic-metamorphic hydrothermal fluids; (c): the superposition of brittle fractures in the later stage leads to the further enrichment of gold and other metal-forming materials, and high-grade gold ore is finally formed at the superposition of strong ductile deformation and brittle fractures.

7. Conclusions

The Xinjiazui gold deposit is located in the northeastern section of back Longmenshan orogenic belt. The Yanzibian–Huashigou shear zone strictly controls the ore mineralization, and high-grade gold ore is developed only in the position with strong ductile deformation and brittle fracture, implying structural control of gold mineralization. Moreover, the host rock of the Xinjiazui gold deposit is composed of $S_{1-2}M$ phyllite and E_1n carbon-silicon-slate, indicating that the gold mineralization is not selective to the stratum. The mineralization of primary ores in the Xinjiazui gold deposit is dominated by quartz-vein-

type gold ores, and gold is mainly hosted by pyrite, occurring as fracture gold or gold inclusions. In addition, the H–O isotopes of quartz suggest that the ore-forming fluids were derived originally from metamorphic fluid. The $\delta^{34}\text{S}$ value and lead isotopes of pyrite show that the ore-forming elements were derived mainly from low-grade metamorphic sedimentary rock. Above all, the Xinjiazui gold deposit is considered an orogenic gold deposit.

Supplementary Materials: The following supporting information can be downloaded at: <https://www.mdpi.com/article/10.3390/min12060688/s1>, Table S1: Electron probe analyses of different types of pyrites in the Xinjiazui gold deposit.

Author Contributions: J.L., X.B., Y.G. and K.Y. conceived and designed the ideas; J.L., H.C., S.K. and W.Y. performed the experiments; J.L., X.B., S.K., Z.W., J.H. and Y.Z. analyzed the data; J.L. prepared the original draft; J.L. and X.B. reviewed and edited the draft. All authors have read and agreed to the published version of the manuscript.

Funding: This study was financially supported by the Project of Xi'an Mineral Resources Survey Center, China Geological Survey (ZD20220313), the China Postdoctoral Science Foundation (300204000298), and National Gold Resources Potential Evaluation of China (ZD20220318).

Data Availability Statement: Not applicable.

Acknowledgments: We would like to thank Xiaoxing Zhang, Yuan Tian, and Wendi Guo for their help during the field work, as well as Nan Li and Liqiang Yang for their assistance with final editing of the paper. We are grateful for constructive comments by the anonymous reviewers.

Conflicts of Interest: The authors declare no conflict of interest.

References

1. Weatherley, D.K.; Henley, R.W. Flash vaporization during earthquakes evidenced by gold deposits. *Nature Geosci.* **2013**, *6*, 294–298. [CrossRef]
2. Foster, D.A.; Gray, D.R.; Kwak, T.A.P.; Bucher, M. Chronology and tectonic framework of turbidite-hosted gold deposits in the Western Lachlan Fold Belt, Victoria: $^{40}\text{Ar} - ^{39}\text{Ar}$ results. *Ore Geol. Rev.* **1988**, *13*, 229–250. [CrossRef]
3. Groves, D.I.; Goldfarb, R.J.; Gebre-Mariam, M.; Hagemann, S.G.; Robert, F. Orogenic gold deposits: A proposed classification in the context of their crustal distribution and relationship to other gold deposit types. *Ore Geol. Rev.* **1998**, *13*, 7–27. [CrossRef]
4. Goldfarb, R.J.; Groves, D.I.; Gardoll, S.J. Orogenic gold and geologic time: A global synthesis. *Ore Geol. Rev.* **2001**, *18*, 1–75. [CrossRef]
5. Goldfarb, R.J.; Qiu, K.F.; Deng, J.; Chen, Y.J.; Yang, L.Q. Orogenic Gold Deposits of China. *SEG Spec. Publ.* **2019**, *22*, 263–324.
6. Goldfarb, R.J.; Groves, D.I. Orogenic gold: Common or evolving fluid and metal sources through time (Review). *Lithos* **2015**, *233*, 2–26. [CrossRef]
7. Qiu, K.F.; Goldfarb, R.J.; Deng, J.; Yu, H.C.; Gou, Z.Y.; Ding, Z.J.; Wang, Z.K.; Li, D.P. Gold deposits of the Jiaodong Peninsula, eastern China. *SEG Spec. Publ.* **2020**, *23*, 753–773.
8. Qiu, K.F.; Yu, H.C.; Deng, J.; McIntire, D.; Gou, Z.Y.; Geng, J.Z.; Chang, Z.S.; Zhu, R.; Li, K.N.; Goldfarb, R.J. The giant Zaozigou orogenic Au–Sb deposit in West Qinling, China: Magmatic or metamorphic origin? *Min. Dep.* **2020**, *55*, 345–362. [CrossRef]
9. Ma, J.; Lv, X.B.; Escolme, A.; Li, S.; Zhao, N.L.; Cao, X.F.; Zhang, L.J.; Lu, F. In-situ sulfur isotope analysis of pyrite from the Pangjiahe gold deposit: Implications for variable sulfur sources in the north and south gold belt of the South Qinling orogeny. *Ore Geol. Rev.* **2018**, *98*, 38–61. [CrossRef]
10. Liang, J.L.; Li, J.; Sun, W.D.; Zhao, J.; Zhai, W.; Huang, Y.; Song, M.C.; Ni, S.J.; Xiang, Q.R.; Zhang, J.C. Source of ore-forming fluids of the Yangshan gold field, western Qinling orogen, China: Evidence from microthermometry, noble gas isotopes and in situ sulfur isotopes of Au-carrying pyrite. *Ore Geol. Rev.* **2019**, *105*, 404–422. [CrossRef]
11. Yang, L.Q.; Deng, J.; Wang, Z.L.; Guo, L.N.; Li, R.H.; Groves, D.I.; Danyushevsky, L.V.; Zhang, C.; Zheng, X.L.; Zhao, H. Relationships between gold and pyrite at the Xincheng gold deposit, Jiaodong Peninsula, China: Implications for gold source and deposition in a brittle epizonal environment. *Econ. Geol.* **2016**, *111*, 105–126. [CrossRef]
12. Liu, H.M.; Beaudoin, G.; Makvandi, S.; Jackson, S.E.; Huang, X.W. Multivariate statistical analysis of trace element compositions of native gold from orogenic gold deposits: Implication for mineral exploration (Article). *Ore Geol. Rev.* **2021**, *131*, 104061. [CrossRef]
13. Deng, J.; Wang, Q.F.; Li, G.J.; Zhao, Y. Structural control and genesis of the Oligocene Zhenyuan orogenic gold deposit, SW China. *Ore Geol. Rev.* **2015**, *65*, 42–54. [CrossRef]
14. Groves, D.I.; Goldfarb, R.J.; Robert, F.; Hart, C.J.R. Gold deposits in metamorphic belts: Overview of current understanding, outstanding problems, future research, and exploration significance. *Econ. Geol.* **2003**, *98*, 1–29.

15. Groves, D.I.; Santosh, M. The giant Jiaodong gold province: The key to a unified model for orogenic gold deposits? *Geosci. Front.* **2016**, *7*, 409–417. [\[CrossRef\]](#)
16. Cook, N.J.; Ciobanu, C.L.; Mao, J.W. Textural control on gold distribution in As-free pyrite from the Dongping, Huangtuliang and Hougou gold ore deposits, North China Craton (Hebei Province, China). *Chem. Geol.* **2009**, *264*, 101–121. [\[CrossRef\]](#)
17. Yan, Y.T.; Li, S.R.; Jia, B.J.; Zhang, N.; Yan, L.N. Composition typomorphic characteristics and statistic analysis of pyrite in gold deposits of different genetic types. *Earth Sci. Front.* **2012**, *19*, 214–226.
18. Belousov, I.; Large, R.R.; Meffre, S.; Danyushevsky, L.V.; Steadman, J.; Beardsmore, T. Pyrite compositions from VHMS and orogenic Au deposits in the Yilgarn Craton, Western Australia: Implications for gold and copper exploration (Review). *Ore Geol. Rev.* **2016**, *79*, 474–499. [\[CrossRef\]](#)
19. Arehart, G.B. Characteristics and origin of sediment-hosted disseminated gold deposits: A review. *Ore Geol. Rev.* **1996**, *11*, 383–403. [\[CrossRef\]](#)
20. Chang, Z.S.; Large, R.R.; Maslennikov, V. Sulfur isotopes in sediment-hosted orogenic gold deposits: Evidence for an early timing and a seawater sulfur source. *Geology* **2008**, *36*, 971–974. [\[CrossRef\]](#)
21. Large, R.R.; Danyushevsky, L.; Hollit, C.; Maslennikov, V.; Meffre, S.; Gilbert, S.; Bull, S.; Scott, R.; Emsbo, P.; Thomas, H.; et al. Gold and trace element zonation in pyrite using a laser imaging technique: Implications for the timing of gold in orogenic and Carlin-style sediment-hosted deposits. *Econ. Geol.* **2009**, *104*, 635–668. [\[CrossRef\]](#)
22. Ulrich, T.; Long, D.G.F.; Kamber, B.S.; Whitehouse, M.J. In situ trace element and sulfur isotope analysis of pyrite in a Paleoproterozoic gold placer deposit, Pardo and Clement Townships, Ontario, Canada. *Econ. Geol.* **2011**, *106*, 667–686. [\[CrossRef\]](#)
23. Chen, L.; Li, X.H.; Li, J.W.; Hofstra, A.H.; Liu, Y.; Koenig, A.E. Extreme variation of sulfur isotopic compositions in pyrite from the Qiuling sediment-hosted gold deposit, West Qinling orogen, central China: An in situ SIMS study with implications for the source of sulfur (Article). *Min. Dep.* **2015**, *50*, 643–656. [\[CrossRef\]](#)
24. Deng, J.; Wang, C.M.; Bagas, L.; Selvaraja, V.; Jeon, H.; Wu, B.; Yang, L.F. Insights into ore genesis of the Jinding Zn–Pb deposit, Yunnan Province, China: Evidence from Zn and in-situ S isotopes. *Ore Geol. Rev.* **2017**, *90*, 943–957. [\[CrossRef\]](#)
25. Yang, L.Q.; Deng, J.; Li, N.; Zhang, C.; Ji, X.Z.; Yu, J.Y. Isotopic characteristics of gold deposits in the Yangshan gold belt, West Qinling, central China: Implications for fluid and metal sources and ore genesis. *J. Geochem. Explor.* **2016**, *168*, 103–118. [\[CrossRef\]](#)
26. Dehnavi, A.S.; McFarlane, C.R.M.; Lentz, D.R.; Walker, J.A. Assessment of pyrite composition by LA-ICP-MS techniques from massive sulfide deposits of the Bathurst Mining Camp, Canada: From textural and chemical evolution to its application as a vectoring tool for the exploration of VMS deposits. *Ore Geol. Rev.* **2018**, *92*, 656–671. [\[CrossRef\]](#)
27. Fiorentini, M.L.; Bekker, A.; Rouxel, O.; Wing, B.A.; Maier, W.; Rumble, D. Multiple sulfur and iron isotope composition of magmatic Ni–Cu–(PGE) sulfide mineralization from eastern Botswana. *Econ. Geol.* **2012**, *107*, 105–116. [\[CrossRef\]](#)
28. Fiorentini, M.; Beresford, S.; Barley, M.; Duuring, P.; Bekker, A.; Rosengren, N.; Cas, R.; Hronsky, J. District to camp controls on the genesis of komatiite-hosted nickel sulfide deposits, Agnew–Wiluna greenstone belt, Western Australia: Insights from the multiple sulfur isotopes. *Econ. Geol.* **2012**, *107*, 781–796. [\[CrossRef\]](#)
29. Voute, F.; Hagemann, S.G.; Evans, N.J.; Villanes, C. Sulfur isotopes, trace element, and textural analyses of pyrite, arsenopyrite and base metal sulfides associated with gold mineralization in the Patay–Parcoy district, Peru: Implication for paragenesis, fluid source, and gold deposition mechanisms. *Min. Dep.* **2019**, *54*, 1077–1100. [\[CrossRef\]](#)
30. Rye, R.O.; Ohmoto, H. Sulfur and carbon isotopes and ore genesis: A review. *Econ. Geol.* **1974**, *69*, 826–842. [\[CrossRef\]](#)
31. Taylor, H.P. Application of oxygen and hydrogen isotope studies to problems of hydrothermal alteration and ore deposition. *Econ. Geol.* **1973**, *68*, 1210. [\[CrossRef\]](#)
32. Ohmoto, H. Isotope of sulfur and carbon. *Geochem. Hydrothermal Ore Depos.* **1979**, 509–567.
33. Ohmoto, H. Stable isotope geochemistry of ore deposits. *Rev. Mineral. Geochem.* **1986**, *16*, 491–559.
34. Ding, T.P.; Jiang, S.Y. Stable isotope study of the Langshan polymetallic mineral district, Inner Mongolia, China. *Resour. Geol.* **2000**, *50*, 25–38. [\[CrossRef\]](#)
35. Chen, Y.J.; Pirajno, F.; Sui, Y.H. Isotope geochemistry of the Tieluping silver–lead deposit, Henan, China: A case study of orogenic silver-dominated deposits and related tectonic setting. *Min. Dep.* **2004**, *39*, 560–575. [\[CrossRef\]](#)
36. Chen, Y.J.; Pirajno, F.; Sui, Y.H. Geology and D–O–C isotope systematics of Tieluping silver deposit, Henan, China: Implications for ore genesis. *Acta Geol. Sinica* **2005**, *79*, 106–119.
37. Li, Z.C. Composition, Structural Characteristics and Evolution of Back–Longmenshan Orogeny (North Section) in the Northwest Margin of Yangtze Block. Ph.D. Thesis, Chang’an University, Xi’an, China, 1 December 2009. (In Chinese with English Abstract).
38. Wei, L.Y. Geological Characteristics and Genesis of the Dingjialing–taiyangping Gold Metallogenic Belt. Master’s Thesis, Xi’an University of Science and Technology, Xi’an, China, 15 April 2008. (In Chinese with English Abstract).
39. Zhong, J. Geological Characteristics and Genesis of Taiyangping Gold Deposit, Sichuan Province. Master’s Thesis, Southwest University of Science and Technology, Mianyang, China, 28 May 2015. (In Chinese with English Abstract).
40. Fu, Y.Z.; Fang, W.X.; Liu, J.J.; Fan, Y.X.; Guo, M.H.; Jiang, J.Z. Characteristics of Tectonic Lithofacies in Dingjialin–Taiyangping–Dongjiayuan gold ore belt, Shaanxi and Sichuan Provinces. *Geotecton. Metallogenia* **2014**, *38*, 787–801, (In Chinese with English Abstract).
41. Liu, J.; Yang, K.; Zhang, X.X.; Kou, S.L.; Yang, W.; Wang, Z.B.; Tian, Y. Geological characteristics and genesis of the Xinjiazui gold deposit in Back–Longmenshan orogenic belt. *Geoscience* **2022**, *36*, 378–388, (In Chinese with English Abstract).

42. Li, N.; Yang, L.Q.; Groves, D.I.; Li, H.X.; Liu, X.W.; Liu, J.; Ye, Y.; Li, H.R.; Liu, C.X.; Yin, C. Tectonic and district to deposit-scale structural controls on the Ge'erke orogenic gold deposit within the Dashui–Zhongqu District, West Qinling Belt, China. *Ore Geol. Rev.* **2020**, *120*, 103436. [\[CrossRef\]](#)
43. Weislogel, A.L.; Graham, S.A.; Chang, E.Z.; Wooden, J.L.; Gehrels, G.E.; Yang, H.S. Detrital zircon provenance of the Late Triassic Songpan–Ganzi complex: Sedimentary record of collision of the North and South China blocks. *Geology* **2006**, *34*, 97–100. [\[CrossRef\]](#)
44. Pin, C.; Gannoun, A.; Dupont, A. Rapid, simultaneous separation of Sr, Pb, and Nd by extraction chromatography prior to isotope ratios determination by TIMS and MC-ICP-MS. *J. Anal. At. Spectrom.* **2014**, *29*, 1858–1870. [\[CrossRef\]](#)
45. Weiss, D.J.; Kober, B.; Dolgoplova, A.; Gallagher, K.; Spiro, B.; Roux, G.L.; Mason, T.F.D.; Kylander, M.; Coles, B.J. Accurate and precise Pb isotope ratio measurements in environmental samples by MC-ICP-MS. *Int. J. Mass Spectrom.* **2004**, *232*, 205–215. [\[CrossRef\]](#)
46. Gong, B.; Zheng, Y.F.; Chen, R.X. An online method combining a thermal conversion elemental analyzer with isotope ratio mass spectrometry for the determination of hydrogen isotope composition and water concentration in geological samples. *Rapid Commun. Mass Spectrom.* **2007**, *21*, 1386–1392. [\[CrossRef\]](#) [\[PubMed\]](#)
47. Ding, T.P.; Jiang, S.Y.; Wan, D.F. *Silicon Isotope Geochemistry*; Geology Publishing House: Beijing, China, 1994; pp. 6–17. (In Chinese)
48. Large, R.R.; Maslennikov, V.V. Invisible gold paragenesis and geochemistry in pyrite from orogenic and sediment-hosted gold deposits. *Minerals* **2020**, *10*, 339. [\[CrossRef\]](#)
49. Zartman, R.E.; Doe, B.R. Plumbotectonics—the model. *Tectonophysics* **1981**, *75*, 135–162. [\[CrossRef\]](#)
50. McCuaig, T.C.; Kerrich, R. P–T–t–deformation–fluid characteristics of lode gold deposits: Evidence from alteration systematics. *Ore Geol. Rev.* **1998**, *12*, 381–453. [\[CrossRef\]](#)
51. Sun, S.H. *North Sichuan–Gannan Carlin–Type Gold Deposits in China*, 1st ed.; Metallurgical Industry Press: Beijing, China, 2009; pp. 25–29. (In Chinese)
52. Taylor, S.R. Trace element abundances and the chondritic earth model. *Geochim. Cosmochim. Acta* **1964**, *28*, 1989–1998. [\[CrossRef\]](#)
53. Zuo, Q.W. Nano SIMS Sulfur Isotope Studies of Pyrite from an Early Paleozoic Marine Shale: Implications for the Sedimentary Environment. Master's Thesis, China University of Geosciences, Beijing, China, 7 June 2020. (In Chinese with English Abstract).
54. Wu, K.X.; Hu, R.Z.; Bi, X.W.; Peng, J.T.; Tang, Q.L. Ore lead isotopes as a tracer for ore-forming material sources: A review. *Geol. Geochem.* **2002**, *3*, 73–81. (In Chinese with English Abstract).
55. Goldfarb, R.J.; Baker, T.; Dubé, B.; Groves, D.I.; Hart, C.J.R.; Gosselin, P. Distribution, character and genesis of gold deposits in metamorphic terranes. In *Econ. Geol. 100th Anniversary*; Hedenquist, J., Thompson, J.F.H., Goldfarb, R.J., Eds.; Society of Economic Geologists: Littleton, CO, USA, 2005; pp. 407–450.
56. Pitcairn, L.K.; Leventis, N.; Beaudoin, G.; Faure, S.; Guilmette, C.; Dubé, B. A metasedimentary source of gold in Archean orogenic gold deposits. *Geology* **2021**, *49*, 862–866. [\[CrossRef\]](#)
57. Groves, D.I.; Santosh, M.; Deng, J.; Wang, Q.F.; Yang, L.Q.; Zhang, L. A holistic model for the origin of orogenic gold deposits and its implications for exploration. *Min. Dep.* **2020**, *55*, 275–292. [\[CrossRef\]](#)
58. Zheng, Y.F.; Chen, J.F. *Stable Isotope Geochemistry*, 1st ed.; Science Press: Beijing, China, 2000; pp. 177–182.